Predicting cortical bone adaptation to axial loading in the mouse tibia

A.F. Pereira[a,*], B. Javaheri[b], A.A. Pitsillides[b], S.J. Shefelbine[c]

[a]*Department of Bioengineering, Imperial College London, UK*
[b]*Comparative Biomedical Sciences, Royal Veterinary College, London, UK*
[c]*Northeastern University, Boston, MA, USA*

Abstract

The development of predictive mathematical models can contribute to a deeper understanding of the specific stages of bone mechanobiology and the process by which bone adapts to mechanical forces. The objective of this work was to predict, with spatial accuracy, cortical bone adaptation to mechanical load, in order to better understand the mechanical cues that might be driving adaptation.

The axial tibial loading model was used to trigger cortical bone adaptation in C57BL/6 mice and provide relevant biological and biomechanical information. A method for mapping cortical thickness in the mouse tibia diaphysis was developed, allowing for a thorough spatial description of where bone adaptation occurs.

Poroelastic finite-element (FE) models were used to determine the structural response of the tibia upon axial loading and interstitial fluid velocity as the mechanical stimulus. FE models were coupled with mechanobiological governing equations, which accounted for non-static loads and assumed that bone responds instantly to local mechanical cues in an on-off manner.

*Corresponding author
Email address: andrepere@gmail.com (A.F. Pereira)

The presented formulation was able to simulate the areas of adaptation and accurately reproduce the distributions of cortical thickening observed in the experimental data with a statistically significant positive correlation (Kendall's tau rank coefficient $\tau = 0.51$, $p < 0.001$).

This work demonstrates that computational models can spatially predict cortical bone mechanoadaptation to time variant stimulus. Such models could be used in the design of more efficient loading protocols and drugs therapies that target the relevant physiological mechanisms.

Keywords: Bone mechanobiology, functional adaptation, fluid-flow, cortical thickness, mouse tibia

1. Introduction

Bone is a dynamic tissue, responding to changes in mechanical demands by adapting its shape and material properties. These self-optimising properties derive from the formation of new bone under mechanical loads and loss of bone in disuse, a mechanism referred to as Wolff's Law (Frost, 1964). Classic examples of the adaptive effect of skeletal loading in humans include bone loss during exposure to microgravity environments (Cavanagh et al., 2005) or bed rest confinement (Issekutz et al., 1966), and bone mass gain resulting from frequent physical exercise (Haapasalo et al., 2000).

The mechanostat hypothesis by Frost (1964) relies upon a quantitatively-matched adaptive response of bone as a function of loading, considering that there are mechanical stimulus thresholds at which bone tissue responds. This conceptual model delineates the foundations of most of the mathematical models developed to simulate bone adaptation (Beaupré et al., 1990; Carter, 1984; Cowin,

1984; Fernandes and Rodrigues, 1999; Huiskes et al., 2000, 1987; Phillips, 2012; Prendergast, 1997; Webster et al., 2012). Such predictive mathematical models usually rely on numerical methods, namely finite-element analysis (FEA), to calculate mechanical fields in bone that result from external loading. These help to find correlations between the mechanical environment and biological response.

Several mechanical stimuli have been suggested to predict spatial patterns of adaptation of bone tissue, such as strain tensor (Cowin, 1984), daily stress stimulus (Beaupré et al., 1990; Carter, 1984) or strain energy density (Huiskes et al., 1987). Following findings suggesting that load-induced fluid-flow is the likely mechanism for mechanocoupling (Klein-Nulend et al., 1995; Reich and Frangos, 1991; Weinbaum et al., 1994), other authors have introduced Darcy fluid velocity as the mechanical stimulus. Such studies modelled pressure relaxation occurring in the lacunar-canalicular system during loading and showed that it can explain not only space-dependent, but also time-dependent phenomena associated with some load parameters. These were able to take into account the effect of load frequency (Chennimalai Kumar et al., 2012; Kameo et al., 2011; Malachanne et al., 2011) or the insertion of rest periods between load cycles (Pereira and Shefelbine, 2014, 2013). Understanding how loading parameters can be tuned to maximise the adaptive response, will contribute to the development of new non-pharmacological interventions to stimulate bone formation.

To date, few studies have thoroughly examined the spatial arrangement of adapted cortical bone across the entire bone in relation to the mechanical field. In addition, simulations of cortical bone modelling are often tested against experimental data with the representation of a few cross sections, with the calculation of bulk quantities, such as minimum moment of area (Chennimalai Kumar

et al., 2012) or remodelling rate (Malachanne et al., 2011). These approaches lack a thorough spatial representation of *in vivo* and simulated cortical adaptation. Roberts et al. (2009) correlated site-specific distribution of new bone apposition with mechanical signals in an animal study on the synergistic effect of PTH and localised mechanical stress, however this analysis was limited to single cross-sections. An approach where this assessment is done with higher spatial resolution is, therefore, required to fully assess the predictive ability of phenomenological models.

We hypothesise that bone forms in regions of high fluid velocity. The objective of this work was to predict, with spatial accuracy, cortical bone adaptation to mechanical load using fluid flow as the mechano-stimulus, in order to better understand the mechanical cues that might be driving adaptation. We conducted complementary *in vivo* and *in silico* studies. *In vivo* bone formation data was obtained using a murine tibial loading model (De Souza et al., 2005). FE models that simulated the structural response of the loaded mouse tibia were developed and poroelastic theory was considered to estimate load-induced interstitial fluid velocities. These models were coupled to a novel mechanobiological formulation that predicts functional cortical bone thickening based on fluid velocity. We calculated changes in cortical thickness resulting from bone formation in real and simulated adaptation, in order to assess the accuracy of the predictive model.

2. Methods

2.1. Axial loading of the mouse tibia

Six ($N = 6$) 12-week-old female C57BL/6J mice, kept in polypropylene cages, were subjected to 12h cycles of light/dark exposure. All procedures were ap-

proved by the local ethical review board and the UK Home Office.

A non-invasive bone adaptation model in mice was used for this experiment, identical to the one described in the work by De Souza et al. (2005) and shown in Figure 1a. The extrinsic actuator consisted of two vertically aligned cups. The cups were enclosed in a servo-hydraulic materials testing machine (Model HC10, Dartec, Ltd., Stourbridge, UK), with an actuator and a load cell. The right tibia of each specimen was placed in between the cups, while the left limb served as a contralateral non-loaded control.

The natural curvature of the tibia induces bending and transforms the axial loading into a combination of compression and mediolateral bending. This loading model provides measurable amounts of bone formation after two weeks, avoids artefacts that arise from the effects of surgical procedures or skin pressure induced periosteal adaptation (observable in flexural loading protocols, Torrance et al. 1994), and allows for the examination of periosteal, endosteal and trabecular adaptation (De Souza et al., 2005).

Load cycles consisted in a 0.1 s trapezoidal load, in which peak loads of 13 N were applied for 0.05 s, with loading and unloading times of 0.025 s, separated by a 9.9 s baseline rest period (De Souza et al., 2005; Poulet et al., 2011). These were applied at 40 cycles/day, three times a week for 2 weeks. Previous studies have shown that loads of 9–11 N elicit lamellar bone adaptation (De Souza et al., 2005; Weatherholt et al., 2013).

Tibiae of both left and right legs were carefully dissected, fixed in 70% EtOH and stored until scanning. We used the Skyscan 1172 μCT system (Skyscan, Kontich, Belgium) with the X-ray tube operated at 50 kV and 200 μA, 1600 ms exposure time with a 0.5 mm aluminium filter and a focal spot size of 5 μm. The slices

PeerJ PrePrints | https://dx.doi.org/10.7287/peerj.preprints.1140v3 | CC-BY 4.0 Open Access | rec: 4 Aug 2015, publ: 4 Aug 2015

were then reconstructed using NRecon 1.6.9.4 (Skyscan, Kontich, Belgium). The μCT transverse images were imported to an image-processing software (Mimics v15.1, Materialise, Leuven, Belgium) where the tibia was segmented from other regions containing pixels belonging to the femur and pes bones. `STL` meshes of right tibiae were reflected and registered to the correspondent contralateral bone using Mimics 'Point Registration' option.

Both geometries were then aligned to the longitudinal axis, parallel to the line that passes through the tibia-fibula proximal and distal junction points. Dimension Z was considered to have the same direction and to be the axial range between the tibia-fibula proximal and distal junctions, in the distal direction ($Z = 0$ at the proximal junction and $Z = 1$ distally), as illustrated in Figure 1b. Cross-sectional images, perpendicular to the Z axis, were exported as `BMP` files and used to calculate the cortical thickness, as described below. Figure 1c–e shows the tibial cross-sections of loaded (black line) and contralateral (grey line) limbs for an example specimen.

Four major anatomical landmarks are present in the diaphysis of the mouse tibia: the interosseous crest (labelled in Figure 1c–e as IC), the tibial ridge (TR), the soleal line (SL) and the proximal crest (PC) (Bab et al., 2007). The left limb tibia (non-loaded leg) was used in the finite element (FE) simulations in subsection 2.4.

2.2. Determining changes in cortical thickness from in vivo experiments

Transverse images of the bone (Figure 2a) and MATLAB (Mathworks, Natick, MA, USA) scripts were used to obtain a map of cortical thickness changes, from contralateral to loaded leg, that occur in the diaphysis of the tibia only, without considering the fibula. The automatic process started by segmenting tibial cortical

PeerJ PrePrints | https://dx.doi.org/10.7287/peerj.preprints.1140v3 | CC-BY 4.0 Open Access | rec: 4 Aug 2015, publ: 4 Aug 2015

bone from the fibula and unconnected trabecular structures. The exterior boundaries were identified and other features resulting from blood vessel and distinct porosities were removed (Figure 2b). The thickness of cortical bone, in this study denoted as Th, was determined at each pixel in the periosteal boundary as the shortest distance to the endosteal boundary (Figure 2c).

Local thickness measurements were arranged into groups according to their angular positions θ from the centroid of the cross-section. For each group the measured thicknesses were averaged for the pixels enclosed within an azimuthal range of $\pi/90$ (2°). Left and right leg results were expressed in a cylindrical coordinate system (Th, θ, Z), illustrated in Figure 3, where the coordinates respectively correspond to the thickness of the cortical shell, the angular position in the cross section with the cortical centroid as origin and the longitudinal distance between the tibia-fibula proximal and distal junctions. The variation of cortical thickness shell ($\Delta Th/Th$) between adapted and non-adapted tibiae, at angle θ and longitudinal position Z, is given by

$$\Delta Th/Th\ (\theta, Z) = \frac{Th_R(\theta, Z) - Th_L(\theta, Z)}{Th_L(\theta, Z)} \tag{1}$$

with Th_L and Th_R as the thickness values of the left and right legs.

Different animals had slight differences in the longitudinal and angular position of the tibial borders and other bony landmarks. However these were enough to make statistical analysis of experimental data results rather challenging, concealing the desired adaptation patterns. We measured changes in second moment of area in tibial cortical bone for all samples (Supplementary Figure S1) [1] and

[1] As shown in Supplementary Figure S1a, the finite element model indicated that tibial loading induced bending around an axis very similar to the geometric minor axis. Therefore, adaptive

PeerJ PrePrints | https://dx.doi.org/10.7287/peerj.preprints.1140v3 | CC-BY 4.0 Open Access | rec: 4 Aug 2015, publ: 4 Aug 2015

identified the one with the smallest least squared error distance from the average. We assumed this sample to be the best representation of average adaptation seen in our experiments. We measured cortical thickness, Th, in the representative sample and its unloaded limb geometry was used as initial state in the adaptation model.

2.3. *Proposed mechanobiological model*

An organ scale predictive model of bone adaptation was developed to include non-static loading conditions, while considering load-induced interstitial fluid velocity as mechanical signal. Adaptation of bone to a mechanical stimulus was determined with a trilinear curve, with high and low mechanical signals inducing respectivelly formation and resorption of bone, and a 'lazy zone' where bone formation and resorption are balanced (Figure 4; Carter 1984; Cowin 1984; Huiskes et al. 1987).

Coupling time integration (or time averaging) of the mechanical signal with previously published stimulus–adaptation relationships (Chennimalai Kumar et al., 2012; Kameo et al., 2011; Malachanne et al., 2011) resulted in excessive qualitative differences in the amount of surface modeling between regions of high and low signal, which were not seen in experimental results. We adjusted the slopes of the remodelling curve (Figure 4a) and imposed a maximum and minimum remodeling rates (Figure 4b) to obtain regions of bone formations that correlated with experimental results. The closest predictions, in terms of spatial locations across the entire tibial shaft and relative amounts of adaptation, when compared with experimental results, were obtained with a step function profile

changes are more likely to be measured around the minor axis.

PeerJ PrePrints | https://dx.doi.org/10.7287/peerj.preprints.1140v3 | CC-BY 4.0 Open Access | rec: 4 Aug 2015, publ: 4 Aug 2015

(Figure 4c). Therefore, our model assumes that, at specific time instances, bone responds to local mechanical cues in an on-off manner and that this response is integrated in time.

The course of action of the presented adaptation model, schematised in Figure 5 for a case where only bone formation is considered, is as follows. For the duration of a load cycle, non-static loading conditions result in varying mechanical signal Ψ values in time. The stimulus Ψ is converted into a discrete value, denoted as Λ, that corresponds to the cellular sensorial output to the mechanical signal. The adaptation rate, $\dot{u}$, is obtained from the time-integration of the cellular signal, finally resulting in bone surface modelling.

The mechanosensing signal calculated at node n and time instant t, $\Psi(n,t)$, can elicit three discrete responses of bone activity, $\Lambda(n,t)$, dictated by the relative value of the signal compared to the apposition and resorption limits of the homeosteatic interval, Ψ_A and Ψ_R. The value of Λ is a dimensionless quantity and can be expressed as the following set of equations

$$\Lambda(n,t) = \begin{cases} 1, & \Psi_A \leq \Psi(n,t) & \text{bone apposition} \\ 0, & \Psi_R \leq \Psi(n,t) < \Psi_A & \text{no net response} \\ -1, & \Psi(n,t) < \Psi_R & \text{bone resorption} \end{cases} \tag{2}$$

Λ takes positive values at time periods where the mechanical signal is above the apposition set point Ψ_A. The corresponding local remodelling rate $\dot{u}$ (units of length per iteration) is linearly proportional to the integral of Λ over time

$$\dot{u}(n) = C \int_t \Lambda(n,t)\ \mathrm{d}t \tag{3}$$

where C is a proportionality constant (units of length per iteration). This means that remodelling rate will be higher the longer the signal stays above the threshold.

PeerJ PrePrints | https://dx.doi.org/10.7287/peerj.preprints.1140v3 | CC-BY 4.0 Open Access | rec: 4 Aug 2015, publ: 4 Aug 2015

The arrangement of the osteocyte network suggests that mechanotransductive signals are transmitted spatially. This communication was modelled similarly to Chennimalai Kumar et al. (2012) by averaging the local adaptive response, $\dot{u}(n)$, over a spherical zone of influence of radius R. Averaging was weighted with function $w(r)$ (Adachi et al., 2001), which linearly decays with distance r from the node where adaptation is being computed

$$w(r) = \frac{(R - r)}{R} \tag{4}$$

The value of R was set to be 150 µm, the average osteon radius (Brockstedt et al., 1996), since it was assumed that the latter is associated with the physical limits of nutrient perfusion and osteocyte action reach [2].

The averaging at a node n, $\bar{\dot{u}}(n)$, was calculated as the mean between the value of $\dot{u}(n)$ and its weighted average at the other nodes inside the zone of influence

$$\bar{\dot{u}}(n) = \frac{1}{2}\left(\dot{u}(n) + \frac{\int_\Omega w(r)\,\dot{u}(r)\ \mathrm{d}\Omega}{\int_\Omega w(r)\ \mathrm{d}\Omega}\right) \tag{5}$$

with Ω as a spherical region of integration, centred in n and excluding its centre.

The vector of nodal displacement rate $\dot{\mathbf{u}}$, with the same direction as the node normal (as bone formation occurs by appositional growth), constitutes the final adaptive quantity to be calculated at the end of each remodelling iteration.

$$\dot{\mathbf{u}}(n) = \bar{\dot{u}}(n)\ \mathbf{n}(n) \tag{6}$$

[2] Interestingly both average (≈ 150 µm) and maximum (≈ 350 µm) values of cortical thickness in mice (apart from the tibial ridge regions) had similar values to the ones observed in osteon radius (Cattaneo et al., 1999). Mouse bones do not have osteons, which may limit their physiologically allowed thicknesses.

PeerJ PrePrints | https://dx.doi.org/10.7287/peerj.preprints.1140v3 | CC-BY 4.0 Open Access | rec: 4 Aug 2015, publ: 4 Aug 2015

2.4. *Adaptation algorithm and FE model*

Poroelastic theory was used to model the biphasic nature of bone and predict fluid motion inside the lacunar canalicular pores (Cowin, 1999). Finite-element (FE) modelling was employed to provide a numerical solution to the poroelastic problem.

Simulations of cortical bone adaptation (Figure 6) iteratively executed the following steps: (1) generate a FE mesh of the unloaded limb, (2) determine the relevant mechanical fields experienced by cortical bone during experimental loading conditions (in this study fluid velocity is considered the mechanical stimulus, $\Psi = V$), (3) apply the adaptation model described in subsection 2.3, (4) update the geometry of bone accordingly.

The solver was run in the High Performance Computing facility at Imperial College London. FE model generation and handling (steps 1 and 4) were implemented using Abaqus (v6.12, ABAQUS Inc., Pawtucket, RI, USA) Python-based scripting extension. MATLAB was used to post-process the FE results and calculate the remodelling rate (step 3).

Only 0.5 s of total loading time were processed, in order to have feasible computation times, enclosing a single load cycle (0.1 s) and allowing pressure relaxation to take place in the remainder 0.4 s. The solver time step was set to 0.005 s, in order to account for the load cycle profile, totaling 100 time frames per loading cycle.

2.4.1. *Material properties*

The mouse tibia was modelled using four material sections, shown in Figure 7a; elastic and poroelastic cortical bone, fibular growth plate and membrane layers (not shown). Cortical bone elements were modelled as transversely

PeerJ PrePrints | https://dx.doi.org/10.7287/peerj.preprints.1140v3 | CC-BY 4.0 Open Access | rec: 4 Aug 2015, publ: 4 Aug 2015

isotropic, linear elastic and homogeneous (Steck et al., 2003a). Elements within the fibular growth plate were assumed to be cartilage, modelled as isotropic (Lacroix and Prendergast 2002 [3]). Predicted surface strains were compared against experimental data, obtained in a previous study by Sztefek et al. (2010), acquired using digital image correlation (DIC) and strain gauges, in 8 week old mice of the same strain and gender.

The poroelastic region (tibial diaphysis in Figure 7a) was defined as the elements enclosed within and surrounding the adaptive region. Elastic elements were considered in the rest of the cortical region (blue colour in Figure 7a), where no adaptation was considered. Intrinsic permeability in the poroelastic bone regions was set to $k = 10^{-22}\,\mathrm{m}^2$ (Pereira and Shefelbine, 2014). Osteocyte canaliculi are predominantly oriented longitudinally, rather than transversely (Dillaman et al., 1991), and, therefore, this value was assigned to the longitudinal component, k_l. Permeability in other directions was assumed to be 10 times smaller. We modelled permeability through the periosteal and endosteal membranes by including a layer of poroelastic elements, similar to Steck et al. (2003a), and considered each surface to have an isotropic permeability of $k = 10^{-17}\,\mathrm{m}^2$ (Evans et al., 2013). The arrangement of membrane layers is not representative, as a much larger thickness was required to obtain good quality elements; however, this membrane thickness did not affect the mechanical stimulus in the bone, Ψ.

The material properties used for bone, fibular growth plate and membrane layers sections are listed in Table 1. The properties for the interstitial fluid, listed

[3]The Poisson ration value used in this study is more appropriate for poroelastic cartilage. However a study was conducted that showed that considering an incompressible growth plate, with $\nu_\mathrm{t} = \nu_\mathrm{lt} = 0.49$, leads to minor changes in the mechanical environment of the diaphysis.

PeerJ PrePrints | https://dx.doi.org/10.7287/peerj.preprints.1140v3 | CC-BY 4.0 Open Access | rec: 4 Aug 2015, publ: 4 Aug 2015

in Table 2, were assumed to be similar to saline. Some of the used constitutive values were estimated or measured for different specimens, as the literature lacks estimation of some poroelastic parameters in murine bone.

Table 1: Material properties used for cortical bone, membrane layers and growth plate elements.

Property		Units	Bone	Memb.	Gr. Pl.
Longitudinal Young Modulus	E_z	MPa	17.0×10^3 †	2 ‡	10.0 ‡
Transverse Young Modulus	E_t	MPa	11.5×10^3 †	2 ‡	10.0 ‡
Transverse Poisson's ratio	ν_t	–	0.38 †	0.167 ‡	0.167 ‡
Longitudinal-transverse Poisson's ratio	ν_{lt}	–	0.41 †	0.167 ‡	0.167 ‡
Transverse shear modulus	G_t	MPa	4.1×10^3 †	0.73 ‡	6.86 ‡
Longitudinal-transverse shear modulus	G_{lt}	MPa	5.2×10^3 †	0.73 ‡	6.86 ‡
Pore volume fraction	ϕ	%	5 ⋆	0.8 ‡	–
Longitudinal permeability	k_l	m^2	1×10^{-22} ^	1×10^{-17} §	–
Transverse permeability	k_t	m^2	1×10^{-23} ^¶	1×10^{-17} §	–
Effective stress coefficient	α	–	0.14 ⋆	–	–

⋆ Cowin (1999), § Evans et al. (2013), ‡ Lacroix and Prendergast (2002),

^ Pereira and Shefelbine (2014), † Steck et al. (2003a), ¶ Dillaman et al. (1991)

Sensitivity studies (not included in this paper) were conducted to determine the influence of trabecular bone and growth plate stiffness on the calculations of the mechanical environment in the diaphysis. A wide interval of stiffness values was considered for each compartment, ranging from cartilage (10MPa) to cortical bone (17GPa). Estimations of Ψ were insensitive to the properties of the tibial growth plate (which is present even in skeletally mature mice), epiphyseal and metaphyseal trabecular bone. Hence, the growth plate and epiphysis were mod-

PeerJ PrePrints | https://dx.doi.org/10.7287/peerj.preprints.1140v3 | CC-BY 4.0 Open Access | rec: 4 Aug 2015, publ: 4 Aug 2015

Table 2: Interstitial fluid material properties (adapted from Cowin 1999).

Property		Units	Fluid
Specific weight	γ	N/m^3	9.8×10^3
Dynamic viscosity	μ	Pa.s	8.9×10^{-4}
Bulk modulus	K_f	MPa	2.3×10^3

elled as solid bone ($E = 17$GPa) and the metaphyseal trabecular compartment was modelled as hollow. The mechanical fields obtained in the fibula were, however, influenced greatly by the material properties of the fibular growth plate, which was modelled as a cartilage layer ($\approx 3.5\,\mu$m thick with modulus $E = 10$MPa).

2.4.2. FE mesh

Using the segmented images from subsection 2.1, the shrink-wrap meshing tool was employed to close small openings and apply smoothing to the geometry, set with a smallest detail of 50 µm and a gap closing distance of 200 µm, followed by a triangle reduction with a tolerance of 10 µm and an edge angle of 30°. The obtained surface mesh was then remeshed using the `Height/Base(N)` shape measurement, a maximum geometric error of 10 µm and a maximum triangle edge length of 30 µm. The final surface mesh, consisting on two shells (representing the endosteal and periosteal surfaces), was exported and used as starting template for our adaptation algorithm.

Surface normal vectors at each node n, $\mathbf{n}(n)$, were calculated as the normalised average of the normals of the triangular elements that contain node n. Normal directions for periosteal and endosteal boundaries were defined, respectively, as

the outer-pointing and the inward-pointing.

Elastic and poroelastic regions, shown in Figure 7a, were respectively meshed with `C3D10` (3D, 10-node tetrahedral quadratic) and `C3D10MP` (with a pore pressure degree of freedom) elements. The volume was remeshed at the start of each iteration of the adaptation algorithm, maintaining the same surface nodes and prolonging mesh quality. The poroelastic section of the initial volume mesh had a distance between closest nodes between 13 and 112 μm, with an average distance of 47.39 μm.

2.4.3. Boundary conditions

Loading conditions were determined from a study by Poulet et al. (2011), where μCT imaging was employed to visualise the knee joint during axial loading. Axial loading described in subsection 2.1 was modelled by using concentrated forces distributed by a node set at the proximal condyles and fixing set of nodes at the distal interior articular surface (Figure 7b). The loads resulted in a total of 13 N applied as a single trapezoidal load cycle, with a load and unload time of 0.025 s and a peak load time of 0.05 s, in line with the *in vivo* studies. At each iteration, the direction of the applied forces was vertically aligned with the distal fixed nodes region, in order to avoid unrealistic bending moments.

Layers of elements adjacent to both outer and inner surfaces modelled the flow boundary conditions at the periosteal and endosteal membranes (Steck et al., 2003a). By default, the regions adjacent to the outer surface of the layers had no fluid pressure gradients and, therefore, zero flow condition was imposed in these boundaries.

2.4.4. *Mechanobiological parameters used*

In order to determine the influence of the reference stimulus, Ψ_A, and adjust this parameter to fit the experimental data, five different values for the stimulus threshold were considered, as listed in Table 3. An arbitrary value was used for C (4.45 µm/iteration); a value large enough to have substantial bone formation between consecutive adaptive iterations, yet small enough to avoid over-deformation of the mesh and in the same order of magnitude as the maximum daily mineral apposition rate calculated from the µCT scans (≈ 6.68 µm/day). In this pro-osteogenic model we did not consider resorption ($\Psi_R = 0$). Table 4 shows the rest of the parameters employed in the simulation.

Surface nodes, where adaptation was considered (Figure 7c), had at least 10 nodes within the spherical zone of influence with radius $R = 150$ µm, and, in denser mesh sections, up to 212 nodes were contained. The whole set of surface nodes had an average of neighbour 45.32 nodes.

Table 3: Values used for the bone apposition reference stimulus, Ψ_A.

	1	2	3	4	5
Ψ_A (µm/s)	1.0×10^{-3}	3.0×10^{-2}	6.0×10^{-2}	7.0×10^{-2}	1.0×10^{-1}

Table 4: Values used for the other parameters of the adaptation model.

Property	C (µm/interation)	Ψ_R (MPa)	R (µm)
Value	4.45	0	150

PeerJ PrePrints | https://dx.doi.org/10.7287/peerj.preprints.1140v3 | CC-BY 4.0 Open Access | rec: 4 Aug 2015, publ: 4 Aug 2015

2.4.5. *Changes in morphology*

The adaptive region was restricted to the tibial diaphysis, as shown in Figure 7c. Mechanical signals were rendered into surface node displacements, $\dot{\mathbf{u}}(n)$, in a direction normal to the bone's surface, simulating bone apposition. Geometry changes were accomplished by translocating surface nodes followed by the generation of a new volume mesh. Changes in bone shape were assessed measuring cortical thickening of cross sectional cuts of the resulting mesh morphology, obtained at each iteration. We determined the maximum change in thickness in the adapting region from the experimental data. The maximum change in thickness for the bone modelled was $\Delta Th/Th \approx 0.67$. We stopped iterations when a region in our simulations reached the experimental maximum thickness value.

To assess the accuracy of the cortical adaptation predictions, we used MATLAB to compute the correlation between experimental and computational $\Delta Th/Th$ measurements, for each value of Ψ_{A}. Change in thickness calculations, presented in the following sections, deviate significantly from normal distribution, as tested by the Kolmogorov-Smirnov test ($p < 0.001$). Therefore, we used the Kendall's tau rank correlation coefficient, a non-parametric correlation test, to compare experimental measurements with the results of our predictive model.

3. Results

3.1. *DIC verification of surface strains*

Figure 8 shows the contour plots of the longitudinal strains ϵ_{zz} calculated in the FE predictions against the DIC measurements by Sztefek et al. (2010), for a non-adapted left tibia. The DIC readings were obtained for a 12 N axial load (the experimental protocol applied 13 N) and thus the force in the FE model was

PeerJ PrePrints | https://dx.doi.org/10.7287/peerj.preprints.1140v3 | CC-BY 4.0 Open Access | rec: 4 Aug 2015, publ: 4 Aug 2015

adjusted accordingly, for this verification step.

These plots show inhomogeneous regions of high strain, with tension on the medial surface and compression on lateral side, specifically on the interosseous crest. Qualitatively, FE strain patterns agree well with the experimental measurements, with a slight overestimation in the peak compressive strains. These results encouraged the use of these FE models to estimate the mechanical stimulus for adaptation.

3.2. Mechanical stimulus calculations

Figure 9 shows the contour plots obtained for fluid velocity magnitude at the time of peak load ($t = 0.025$s) in the initial, unadapted geometry. Due to the higher permeability of the membrane, the boundaries at the periosteum and endosteum develop low pore pressures, leading to higher fluid velocity magnitudes in the regions adjacent of the inner and outer surfaces.

Interestingly, the fluid in this model flows in opposite direction to intuitive predictions; the interosseous crest region, which experiences compressive strains, develops low pore pressures during loading (influx of fluid) and high pore pressures during unloading (efflux of fluid). Conversely, the medial surface, in tension, develops pore pressures during loading, then low pore pressures during unloading. This counter-intuitive flow direction is illustrated in Supplementary Figure S2 and is consistent with previous studies (Steck et al., 2003b).

The time-varying profiles of fluid velocity were considered the mechanical stimulus used in the adaptation algorithm and the resulting experimental and simulated changes in bone morphology were compared using positional changes in cortical thickness.

PeerJ PrePrints | https://dx.doi.org/10.7287/peerj.preprints.1140v3 | CC-BY 4.0 Open Access | rec: 4 Aug 2015, publ: 4 Aug 2015

3.3. *In vivo adaptive response*

Second moment of area measurements (Supplementary Figure S1), calculated for all specimens, increased with statistical significance in $Z \in [0.1, 0.7]$ when the loaded limb was compared to the non-loaded limb. This provided evidence for the anabolic effect of mechanical loading.

Figure 10 shows cross-sections of the specimen's tibia (a–c) and respective polar representation of cortical thickness, Th, calculated from μCT images (d–f) and from *in silico* simulations for the optimal value of Ψ_A (g–i), determined in subsection 3.4. These are shown for control (grey line) and adapted (solid line) tibiae, at $Z = 0.3$, 0.5 and 0.7. Figure 11 illustrates the calculations of changes in cortical thickness, $\Delta Th/Th$, with colour maps plotted in a two-dimensional plane (θ, Z).

A common feature is the high thickness values calculated between $\theta = 40$–$60°$, for $Z < 0.7$, a region which corresponds to the tibial ridge and peaks around 1000 μm. The interosseous crest is clearly noticeable as the local maxima around $\theta = 300°$ at all values of Z. The soleal line and the proximal crest are better visible in Figure 10, around $\theta = 220°$ and 160°, respectively.

Bone formation was observed in two regions, the medial surface (roughly between $\theta = 90$–$180°$, where maximum tensile strains were experienced) and the interosseous crest (between $\theta = 240$–$350°$, in compression). Formation in the interosseous crest is present across the whole length of the diaphysis, whereas increase in bone thickness in the medial surface is most noticeable around the mid-diaphysis (Figure 10e).

Some noise was present in the thickness measurements, particularly in proximal regions (Figure 10d) and the tibial ridge. The tibial ridge region is observable

PeerJ PrePrints | https://dx.doi.org/10.7287/peerj.preprints.1140v3 | CC-BY 4.0 Open Access | rec: 4 Aug 2015, publ: 4 Aug 2015

in the colour map in Figure 11a as the horizontal dashes of high $\Delta Th/Th$ values and occasional sudden longitudinal changes in thickness around $\theta = 50°$. The main contributors for the presence of deceptive changes in thickness were (1) trabecular structures that, in some transverse sections, remained connected to cortical shell (Supplementary Figure S3), (2) the opening and closing of foramen, both in the medullar cavity and in the periosteum (Supplementary Figure S4), and (3) small organ-level contralateral morphological differences that lead to a misalignment of correspondent anatomical landmarks. These thickness artefacts were not considered as true adaptation (Supplementary Figure S5).

Most of these features were contained outside the dashed box in Figure 11a, i. e., the region that excludes the tibial ridge, and the proximal crest and the region with more concentration of connected trabecular bone, i. e., the first 15% of length. All regions where a reduction in cortical thickness was obtained were associated with calculation artefacts.

These results confirm that load-related increases in resorption were not found in the *in vivo* data. Cortical thickening calculations provided insights into the adaptive response and better understanding of the effects of external loading. We applied the same methodology to assess whether our computational and mechanobiological models matched these measurements.

3.4. Simulation of adaptation

Table 5 lists the iterations that matched the peak $\Delta Th/Th$ in the regions where bone formation occurred, for the considered values of Ψ_A. Not surprisingly, with a lower threshold, fewer iterations were needed to reach a thickness change of 0.67.

Table 5: Final iteration obtained for each value of stimulus threshold, Ψ_A.

Ψ_A	Iteration
1.0×10^{-3}	7
3.0×10^{-2}	13
6.0×10^{-2}	12
7.0×10^{-2}	13
1.0×10^{-1}	15

Cortical thickness values obtained in this simulation are shown in polar coordinates in Figures 10g–i and in a colour map in Figure 11b. All simulations predicted load-related changes in architecture and increases in bone formation around the interosseous crest and in the medial surface, the regions of high mechanoadaptive response identified in the experimental data. Bone formation was overestimated in the distal half of the medial side (area comprised within $Z > 0.55$ and $90° < \theta < 180°$), as observable in the site marked by the red asterisk in Figures 10f, 10i and 11. Increasing the value of the threshold Ψ_A resulted in a gradual confinement of adaptation to the regions where the measured strain and predicted mechanical stimulus Ψ were highest (i. e., the interosseous crest).

Figure 12 shows, for the different values of Ψ_A, the Kendall's tau value obtained when compared $\Delta Th/Th$ in 10,763 data points contained inside the dashed yellow lines in Figure 11 (in order to exclude the areas with a high concentration of artefacts) with the corresponding region in the simulation data. A value of $\Psi_A = 3 \times 10^{-2}\,\mathrm{m\,s^{-1}}$ gave the best predictions (correlation coefficient $\tau = 0.51$, $p < 0.001$) when compared with the *in vivo* response, showing a significant rela-

PeerJ PrePrints | https://dx.doi.org/10.7287/peerj.preprints.1140v3 | CC-BY 4.0 Open Access | rec: 4 Aug 2015, publ: 4 Aug 2015

tively strong positive correlation.

4. Discussion

The mouse tibial axial compression loading model is commonly used for studying load-induced anabolic effects in bone. We used finite element analysis to determine the structural response of the tibia during mechanical stimulation and used poroelastic theory to estimate interstitial fluid flow. We propose a new mechanobiological formulation to predict cortical bone adaptation that results from non-static loading conditions. We determined the accuracy of our mechanobiological simulations compared to thickness changes quantified with μCT scans of loaded and non-loaded limbs of mice.

4.1. Cortical thickening measurements reveal sites of in vivo bone adaptation

Significant changes in cortical geometry were found between non-loaded and loaded bones, demonstrating the crucial role of mechanics in bone adaptation. The effects of expected daily habitual loading were not taken into consideration, as both legs were assumed to be exposed to similar physical forces during that regime. Previous studies found that surface peak strains, for 13 N applied loads, were up to 10 times higher than during normal walking and up to 5 times higher than during 13 cm jumps (De Souza et al., 2005). Despite the need for further studies that explore the relative contribution of normal cage activity *versus* extrinsic applied loading, these data provide strong evidence for the role of extrinsic mechanical loading as the major contributor for the adaptive response observed in the loaded leg.

The calculation of cortical thickness changes allowed for a comprehensive method for comparison of *in vivo* and *in silico* adaptation. Previous loading mod-

els in murine long bones reported 'how much' bone had formed in a specific cross section, using bulk cross sectional parameters, but not 'where' it has formed in the cross section (De Souza et al., 2005; Main et al., 2014; Robling et al., 2002; Weatherholt et al., 2013; Willinghamm et al., 2010). The method presented here provides spatial patterns of bone formation across the whole diaphysis that can be mapped to those distributions of strains, and other mechanical sequelae, that are engendered by the controlled application of load in this model. The capacity to control and modify these applied loads, together with the scope, shown herein, to map the distribution of the osteogenic response along the entire bone length, provides for added power in these analyses.

Our cortical thickness measurements showed that bone formation takes place predominantly on the medial surface and the interosseous crest, where our model, and experimental strain mapping with DIC, show high tensile and compressive strains. Some expected variability was seen on the location and extent of surface modelling in different samples, likely associated with the adaptation tolerance of each mouse, differential handling, loading of mice or physical activity outside loading times (fighting, cage climbing, etc.) Apart from one mouse, which did not exhibit any noticeable changes in cortical thickness in the whole diaphysis, all loaded tibiae had the highest amounts of bone formation in the interosseous crest, which matched histological regions found in single sections (De Souza et al., 2005). Some studies have shown woven bone response at very high loads using this model (Holguin et al., 2014); none of our mice demonstrated woven bone formation in the tibial shaft.

Measurement artefacts, in our loaded-nonloaded μCT comparisons, were easily identified, allowing focus on the true functional adaptation regions. Further

developments, such as the removal of the effect of trabecular bone and contralateral misalignment, will improve this method. Nonrigid registration of each bone to the contralateral equivalent could be included, as done in previous human hip fracture studies, where regions of cortical thinning were determined (Poole et al., 2012). This would allow statistical comparison of several mice studies and facilitate the examination of thickness maps obtained from μCT scans. An alternative methodology would be time-lapsed imaging of bone morphometry (Lambers et al., 2011), which combines *in vivo* μCT with registration of the same bone at different time points. Yet, the presented methodology, using *ex vivo* specimen imaging of contralateral bones, allows morphology to be compared using images from conventional scanners, which are highly accessible.

4.2. Constitutive assumptions for permeability of bone and membranes

The correct order of magnitude of bone permeability is still a matter of debate (Cardoso et al., 2013). Previous computational studies (Pereira and Shefelbine, 2014) showed that poroelastic models with bone permeability $k = 10^{-22}\,\mathrm{m}^2$ simulate relaxation times similar to *in vivo* measures in mice and consistent with recent experimental estimations (Benalla et al., 2014).

The periosteal and endosteal permeabilities are commonly assumed to be respectively very low and very high, when compared to bone tissue. However, new experimental measurements raise questions regarding the assumption of an impermeable periosteum. Evans et al. (2013) measured ovine periosteal permeability to be higher, in the order of $1 \times 10^{-17}\,\mathrm{m}^2$, for low flow rates, roughly 5 orders of magnitude higher than the permeability of the lacunar-canalicular porosity. The same value was assigned to both surfaces, despite the fact that the literature often characterises the endosteum to be more permeable than the periosteum. However,

due to the considerable offset between lacunar-canalicular and periosteal permeability (5 orders of magnitude), poroelastic models were insensitive to any value of endosteal permeability above 1×10^{-17} m^2.

4.3. Fluid velocity as stimulus for bone adaptation

Darcy fluid velocity was considered as the *local* mechanical stimulus following recent observations that suggest that load-induced fluid-flow is the likely mechanism for mechanocoupling (Klein-Nulend et al., 1995; Reich and Frangos, 1991; Weinbaum et al., 1994). Integrins (Wang et al., 2007), primary cilia (Temiyasathit and Jacobs, 2010), and stretch activated ion channel (Duncan and Turner, 1995) may be involved in transduction of the flow signal to the cell. Two mechanoreception mechanisms have been proposed to explain the role of fluid flow in mechanosignalling (1) fluid shear stress acting on the cell membrane (Klein-Nulend et al., 1995) and (2) fluid drag force acting on the pericellular matrix (PCM) fibres that tether cell transmembrane proteins to proteins in the extracellular matrix (Cowin and Weinbaum, 1998)[4]. According to Weinbaum et al. (1994) and You et al. (2001), the shear forces applied at the osteocyte process, F_s, and the drag forces applied on the transverse pericellular fibres, F_d, both depend on the geometry of canaliculi and cellular processes, the permeability of the extracellular space (dictated by the arrangement of fibres) and the spatial gradient of fluid pressure along the direction of the canaliculi, $\partial p/\partial y$. In our poroelastic model, both the effect of the structural properties of the canaliculi and the intrinsic permeability at the macroscopic level, k, are considered to be homogenised at

[4]Drag forces on the PCM were estimated to be 20 times higher than shear forces (You et al., 2001), suggesting that drag forces may be the most likely mechanosignalling mechanism.

PeerJ PrePrints | https://dx.doi.org/10.7287/peerj.preprints.1140v3 | CC-BY 4.0 Open Access | rec: 4 Aug 2015, publ: 4 Aug 2015

the continuum level. Therefore, the term $\partial p/\partial y$ is the only expected to vary in time and across the bone geometry. Providing these assumptions, F_s and F_d are proportional to each other (You et al., 2001) and proportional to the apparent fluid velocity, V.

$$F_s \propto F_d \propto V. \tag{7}$$

Hence, fluid velocity provides, at the continuum level, a good approximation to both shear and drag forces and should be a suitable mechanical stimulus to simulate adaptation in computational studies.

4.4. Mechanobiological model captured the in vivo bone formation patterns

Our mathematical model was able to accurately predict the areas of adaptation and reproduce the distributions of load-induced cortical thickening observed *in vivo*. The statistically significant and relatively strong correlation of our simulations with the measured data suggest that our model is suitable to predict cortical bone adaptation in the murine loading model and that poroelastic models can be used to understand a possible link between fluid flow and loading parameters, at the organ level. The simulations were most accurate in the mid-diaphysis and less accurate proximally, due to the artefacts in the experimental measurements. There were also small discrepancies in the distal half of the medial side as indicated in Figures 10 and 11, likely due to inevitable simplifications in our approach, such as homogeneous constitutive and mechanobiological assumptions (such as threshold stimuli, and osteocyte distribution), loading conditions and implicit modelling of biochemical processes.

The presented mechanobiological model is proposed as a time-dependent analogy to the trilinear curve referred in subsection 2.3. Trilinear stimulus–

PeerJ PrePrints | https://dx.doi.org/10.7287/peerj.preprints.1140v3 | CC-BY 4.0 Open Access | rec: 4 Aug 2015, publ: 4 Aug 2015

adaptation functions are commonly used in bone adaptation studies (Adachi et al., 2001; Beaupré et al., 1990; Carter, 1984; Chennimalai Kumar et al., 2012; Cowin, 1984; Huiskes et al., 1987), based on various of studies showed there is a dose-dependent relationship between higher mechanical stimulation and bone formation response (Bacabac et al., 2004; Rubin and Lanyon, 1984; Turner et al., 1994). In this study, we adjusted the stimulus–adaptation relationship, exploring different slopes and thresholds for bone formation, leading to a step-function profile that suggests a discrete instantaneous response from bone cells. This does not necessarily mean that osteoblasts are not capable of proportionally adjust their response to mechanical signal. One could hypothesise that bone cells integrate discrete signals over time that result in a continuous tissue response.

The mechanical stimulus threshold for bone accretion, Ψ_A (and, if modelled, the threshold for resorption, Ψ_R), dictates the spatial extent of the adaptive region. The lower its value, the more sites will respond to the loading, and thus the larger this region will be. Regions exposed for longer periods to mechanical stimulus, will build up higher amounts of formed tissue, integrating non-static load conditions. As a result, Ψ_A also regulates the amount of added bone. Biologically, both threshold values Ψ_A and Ψ_R are likely to be regulated by multiple factors, such as the cellular network, metabolic and nutrient availability, or the local material properties of bone, and may not be constant within bone tissue.

Using a fluid-related stimulus captures the influence of the time dependence of adaptation, specifically the effects of load rate, frequency (Chennimalai Kumar et al., 2012; Kameo et al., 2011; Malachanne et al., 2011) and rest periods between load cycles (Pereira and Shefelbine, 2014, 2013). Strain and stress, used as mechanical stimuli for adaptation, are insensitive to these parameters. Yet fluid-

PeerJ PrePrints | https://dx.doi.org/10.7287/peerj.preprints.1140v3 | CC-BY 4.0 Open Access | rec: 4 Aug 2015, publ: 4 Aug 2015

flow as a mechanical stimulus is not capable of modelling long-term saturation in the functional adaptation of bone mass for increasing number of load cycles per day (Burr et al., 2002) or the recovery of mechanosensitivity in protocols that include rest-insertion periods in the order of hours (Robling et al., 2001) or days (Saxon et al., 2005). Future work will extend this, by examining how cells desensitise following persistent mechanostimulation, in the longer term. In addition, further developments of this study will look at how the presented adaptation law translates to different animal models, ages and load parameters.

This is the first time, to our knowledge, that a cortical bone adaptation model has been accurately predicted with 3D spatial resolution. The ability to locally predict where bone will form under a given mechanical load has implications for optimising non-pharmacological therapies that direct bone adaptation with mechanical loads. This can potentially contribute to the integration of poroelastic formulations in a multi-scale framework of load-induced bone adaptation. This model will utilise this capability in future studies to optimise the loading regime. The shift from postdictive to predictive models will empower researchers to understand where and how much bone will form under defined loading conditions, which eventually will enable clinicians in the design of optimised external loads or exercise regimes that are able to address bone deficits in clinical diagnoses linked to bone loss.

Data accessibility

Data deposited in the GitHub repository: `https://github.com/afpereira/mouseTibiaData` .

Acknowledgements

This work was supported by Fundação para a Ciência e a Tecnologia (FCT, PhD grant SFRH/BD/62840//2009) and the Biotechnology and Biological Sciences Research Council (BBSRC, grant BB/I014608/1).

Author Contributions

AFP conceived, designed and implemented the predictive model, analysed and interpreted the complete data, wrote the paper, prepared figures and tables and reviewed drafts of the paper; **BJ** designed and performed the animal loading, analysed and interpreted experimental data, reviewed drafts of the paper; **AAP** conceived and designed the animal loading experiments, analysed and interpreted the complete data, contributed to materials and reviewed drafts of the paper; **SJS** conceived and designed animal loading experiments, conceived and designed the predictive model, analysed and interpreted the complete data, contributed materials and software licences, reviewed drafts of the paper. All authors gave final approval for publication.

References

Adachi, T., Tsubota, K.-i., Tomita, Y., Hollister, S. J., Apr. 2001. Trabecular Surface Remodeling Simulation for Cancellous Bone Using Microstructural Voxel Finite Element Models. Journal of Biomechanical Engineering 123 (5), 403–409.

Bab, I., Hajbi-Yonissi, C., Gabet, Y., Müller, R., 2007. Tibio-Fibular Complex and Knee Joint. In: Micro-Tomographic Atlas of the Mouse Skeleton. Springer US, pp. 171–181.

PeerJ PrePrints | https://dx.doi.org/10.7287/peerj.preprints.1140v3 | CC-BY 4.0 Open Access | rec: 4 Aug 2015, publ: 4 Aug 2015

Bacabac, R. G., Smit, T. H., Mullender, M. G., Dijcks, S. J., Van Loon, J. J., Klein-Nulend, J., Mar. 2004. Nitric oxide production by bone cells is fluid shear stress rate dependent. Biochemical and Biophysical Research Communications 315 (4), 823–829.

Beaupré, G. S., Orr, T. E., Carter, D. R., 1990. An approach for time-dependent bone modeling and remodeling - application: A preliminary remodeling simulation. Journal of Orthopaedic Research 8 (5), 662–670.

Benalla, M., Palacio-Mancheno, P., Fritton, S., Cardoso, L., Cowin, S., 2014. Dynamic permeability of the lacunar-canalicular system in human cortical bone. Biomechanics and Modeling in Mechanobiology 13 (4), 801–812.

Brockstedt, H., Bollerslev, J., Melsen, F., Mosekilde, L., Jan. 1996. Cortical bone remodeling in autosomal dominant osteopetrosis: A study of two different phenotypes. Bone 18 (1), 67–72.

Burr, D., Robling, A., Turner, C., May 2002. Effects of biomechanical stress on bones in animals. Bone 30 (5), 781–786.

Cardoso, L., Fritton, S. P., Gailani, G., Benalla, M., Cowin, S. C., 2013. Advances in assessment of bone porosity, permeability and interstitial fluid flow. Journal of Biomechanics 46 (2), 253–265.

Carter, D., Mar. 1984. Mechanical loading histories and cortical bone remodeling. Calcified Tissue International 36, S19–S24.

Cattaneo, C., DiMartino, S., Scali, S., Craig, O., Grandi, M., Sokol, R., Jun. 1999. Determining the human origin of fragments of burnt bone: a comparative

PeerJ PrePrints | https://dx.doi.org/10.7287/peerj.preprints.1140v3 | CC-BY 4.0 Open Access | rec: 4 Aug 2015, publ: 4 Aug 2015

study of histological, immunological and DNA techniques. Forensic Science International 102 (2–3), 181–191.

Cavanagh, P. R., Licata, A. A., Rice, A. J., Jun. 2005. Exercise and pharmacological countermeasures for bone loss during long-duration space flight. Gravitational and space biology bulletin: publication of the American Society for Gravitational and Space Biology 18 (2), 39–58.

Chennimalai Kumar, N., Dantzig, J., Jasiuk, I., 2012. Modeling of cortical bone adaptation in a rat ulna: Effect of frequency. Bone.

Cowin, S., Mar. 1984. Mechanical modeling of the stress adaptation process in bone. Calcified Tissue International 36, S98–S103.

Cowin, S. C., Mar. 1999. Bone poroelasticity. Journal of Biomechanics 32 (3), 217–238.

Cowin, S. C., Weinbaum, S., 1998. Strain Amplification in the Bone Mechanosensory System. The American Journal of the Medical Sciences 316 (3), 184–188.

De Souza, R. L., Matsuura, M., Eckstein, F., Rawlinson, S. C., Lanyon, L. E., Pitsillides, A. A., 2005. Non-invasive axial loading of mouse tibiae increases cortical bone formation and modifies trabecular organization: a new model to study cortical and cancellous compartments in a single loaded element. Bone 37 (6), 810–818.

Dillaman, R. M., Roer, R. D., Gay, D. M., 1991. Fluid movement in bone: Theoretical and empirical. Journal of Biomechanics 24 (Supplement 1), 163–177.

PeerJ PrePrints | https://dx.doi.org/10.7287/peerj.preprints.1140v3 | CC-BY 4.0 Open Access | rec: 4 Aug 2015, publ: 4 Aug 2015

Duncan, R. L., Turner, C. H., Nov. 1995. Mechanotransduction and the functional response of bone to mechanical strain. Calcified Tissue International 57 (5), 344–358.

Evans, S. F., Parent, J. B., Lasko, C. E., Zhen, X., Knothe, U. R., Lemaire, T., Knothe Tate, M. L., 2013. Periosteum, bone's "smart" bounding membrane, exhibits direction-dependent permeability. Journal of Bone and Mineral Research 28 (3), 608–617.

Fernandes, P., Rodrigues, H., 1999. A Model of Bone Adaptation Using a Global Optimisation Criterion Based on the Trajectorial Theory of Wolff. Computer Methods in Biomechanics and Biomedical Engineering 2 (2), 125–138.

Frost, H. M., Jun. 1964. The Laws of Bone Structure. C.C. Thomas.

Haapasalo, H., Kontulainen, S., Sievänen, H., Kannus, P., Järvinen, M., Vuori, I., Sep. 2000. Exercise-induced bone gain is due to enlargement in bone size without a change in volumetric bone density: a peripheral quantitative computed tomography study of the upper arms of male tennis players. Bone 27 (3), 351–357.

Holguin, N., Brodt, M. D., Sanchez, M. E., Silva, M. J., Aug. 2014. Aging diminishes lamellar and woven bone formation induced by tibial compression in adult C57bl/6. Bone 65, 83–91.

Huiskes, R., Ruimerman, R., van Lenthe, G. H., Janssen, J. D., Jun. 2000. Effects of mechanical forces on maintenance and adaptation of form in trabecular bone. Nature 405 (6787), 704–706.

PeerJ PrePrints | https://dx.doi.org/10.7287/peerj.preprints.1140v3 | CC-BY 4.0 Open Access | rec: 4 Aug 2015, publ: 4 Aug 2015

Huiskes, R., Weinans, H., Grootenboer, H. J., Dalstra, M., Fudala, B., Slooff, T. J., 1987. Adaptive bone-remodeling theory applied to prosthetic-design analysis. Journal of Biomechanics 20 (11-12), 1135–1150.

Issekutz, B., Blizzard, J. J., Birkhead, N. C., Rodahl, K., May 1966. Effect of prolonged bed rest on urinary calcium output. Journal of Applied Physiology 21 (3), 1013 –1020.

Kameo, Y., Adachi, T., Hojo, M., Aug. 2011. Effects of loading frequency on the functional adaptation of trabeculae predicted by bone remodeling simulation. Journal of the Mechanical Behavior of Biomedical Materials 4 (6), 900–908.

Klein-Nulend, J., van der Plas, A., Semeins, C., Ajubi, N., Frangos, J., Nijweide, P., Burger, E., Mar. 1995. Sensitivity of osteocytes to biomechanical stress in vitro. The FASEB Journal 9 (5), 441 –445.

Lacroix, D., Prendergast, P., Sep. 2002. A mechano-regulation model for tissue differentiation during fracture healing: analysis of gap size and loading. Journal of Biomechanics 35 (9), 1163–1171.

Lambers, F. M., Schulte, F. A., Kuhn, G., Webster, D. J., Müller, R., Dec. 2011. Mouse tail vertebrae adapt to cyclic mechanical loading by increasing bone formation rate and decreasing bone resorption rate as shown by time-lapsed in vivo imaging of dynamic bone morphometry. Bone 49 (6), 1340–1350.

Main, R. P., Lynch, M. E., Meulen, M. C. H. v. d., May 2014. Load-induced changes in bone stiffness and cancellous and cortical bone mass following tibial compression diminish with age in female mice. The Journal of Experimental Biology 217 (10), 1775–1783.

PeerJ PrePrints | https://dx.doi.org/10.7287/peerj.preprints.1140v3 | CC-BY 4.0 Open Access | rec: 4 Aug 2015, publ: 4 Aug 2015

Malachanne, E., Dureisseix, D., Jourdan, F., 2011. Numerical model of bone remodeling sensitive to loading frequency through a poroelastic behavior and internal fluid movements. Journal of the Mechanical Behavior of Biomedical Materials 4 (6), 849–857.

Pereira, A. F., Shefelbine, S. J., Jan. 2014. The influence of load repetition in bone mechanotransduction using poroelastic finite-element models: the impact of permeability. Biomechanics and Modeling in Mechanobiology 13 (1), 215–225.

Pereira, A. F., Shefelbine, S. S., 2013. Modelling Rest-Inserted Loading in Bone Mechanotransduction Using Poroelastic Finite Element Models: The Impact of Permeability. In: Poromechanics V. American Society of Civil Engineers, pp. 1137–1144.

Phillips, A. T. M., 2012. Structural optimisation: biomechanics of the femur. Proceedings of the ICE - Engineering and Computational Mechanics 165 (Volume 165, Issue 2), 147–154(7).

Poole, K. E. S., Treece, G. M., Mayhew, P. M., Vaculík, J., Dungl, P., Horák, M., Štěpán, J. J., Gee, A. H., Jun. 2012. Cortical Thickness Mapping to Identify Focal Osteoporosis in Patients with Hip Fracture. PLoS ONE 7 (6), e38466.

Poulet, B., Hamilton, R. W., Shefelbine, S., Pitsillides, A. A., Jan. 2011. Characterizing a novel and adjustable noninvasive murine joint loading model. Arthritis and Rheumatism 63 (1), 137–147.

Prendergast, P., Sep. 1997. Finite element models in tissue mechanics and orthopaedic implant design. Clinical Biomechanics 12 (6), 343–366.

PeerJ PrePrints | https://dx.doi.org/10.7287/peerj.preprints.1140v3 | CC-BY 4.0 Open Access | rec: 4 Aug 2015, publ: 4 Aug 2015

Reich, K. M., Frangos, J. A., Sep. 1991. Effect of flow on prostaglandin E2 and inositol trisphosphate levels in osteoblasts. American Journal of Physiology - Cell Physiology 261 (3), C428–C432.

Roberts, M. D., Santner, T. J., Hart, R. T., Nov. 2009. Local bone formation due to combined mechanical loading and intermittent hPTH-(1-34) treatment and its correlation to mechanical signal distributions. Journal of Biomechanics 42 (15), 2431–2438.

Robling, A. G., Burr, D. B., Turner, C. H., Oct. 2001. Recovery periods restore mechanosensitivity to dynamically loaded bone. Journal of Experimental Biology 204 (19), 3389–3399.

Robling, A. G., Hinant, F. M., Burr, D. B., Turner, C. H., 2002. Improved bone structure and strength after long-term mechanical loading is greatest if loading is separated into short bouts. Journal of Bone and Mineral Research 17, 1545–1554.

Rubin, C. T., Lanyon, L. E., 1984. Regulation of bone formation by applied dynamic loads. The Journal of Bone and Joint Surgery 66 (3), 397.

Saxon, L., Robling, A., Alam, I., Turner, C., Mar. 2005. Mechanosensitivity of the rat skeleton decreases after a long period of loading, but is improved with time off. Bone 36 (3), 454–464.

Steck, R., Niederer, P., Knothe Tate, M. L., Jan. 2003a. A Finite Element Analysis for the Prediction of Load-induced Fluid Flow and Mechanochemical Transduction in Bone. Journal of Theoretical Biology 220 (2), 249–259.

PeerJ PrePrints | https://dx.doi.org/10.7287/peerj.preprints.1140v3 | CC-BY 4.0 Open Access | rec: 4 Aug 2015, publ: 4 Aug 2015

Steck, R., Niederer, P., Knothe Tate, M. L., Jun. 2003b. Fluid flows through anisotropic, poroelastic bone models in the opposite direction to that through analogous isotropic models. In: ASME summer bioengineering conference. Key Biscayne, Florida, pp. 213–4.

Sztefek, P., Vanleene, M., Olsson, R., Collinson, R., Pitsillides, A. A., Shefelbine, S., 2010. Using digital image correlation to determine bone surface strains during loading and after adaptation of the mouse tibia. Journal of Biomechanics 43 (4), 599–605.

Temiyasathit, S., Jacobs, C. R., Apr. 2010. Osteocyte primary cilium and its role in bone mechanotransduction. Annals of the New York Academy of Sciences 1192 (1), 422–428.

Torrance, A. G., Mosley, J. R., Suswillo, R. F. L., Lanyon, L. E., Mar. 1994. Noninvasive loading of the rat ulna in vivo induces a strain-related modeling response uncomplicated by trauma or periostal pressure. Calcified Tissue International 54 (3), 241–247.

Turner, C. H., Forwood, M. R., Otter, M. W., Aug. 1994. Mechanotransduction in bone: do bone cells act as sensors of fluid flow? The FASEB Journal: Official Publication of the Federation of American Societies for Experimental Biology 8 (11), 875–878.

Wang, Y., McNamara, L. M., Schaffler, M. B., Weinbaum, S., Oct. 2007. A model for the role of integrins in flow induced mechanotransduction in osteocytes. Proceedings of the National Academy of Sciences 104 (40), 15941–15946.

PeerJ PrePrints | https://dx.doi.org/10.7287/peerj.preprints.1140v3 | CC-BY 4.0 Open Access | rec: 4 Aug 2015, publ: 4 Aug 2015

Weatherholt, A. M., Fuchs, R. K., Warden, S. J., Jan. 2013. Cortical and trabecular bone adaptation to incremental load magnitudes using the mouse tibial axial compression loading model. Bone 52 (1), 372–379.

Webster, D., Wirth, A., Lenthe, G. H. v., Müller, R., Jan. 2012. Experimental and finite element analysis of the mouse caudal vertebrae loading model: prediction of cortical and trabecular bone adaptation. Biomechanics and Modeling in Mechanobiology 11 (1-2), 221–230.

Weinbaum, S., Cowin, S., Zeng, Y., Mar. 1994. A model for the excitation of osteocytes by mechanical loading-induced bone fluid shear stresses. Journal of Biomechanics 27 (3), 339–360.

Willinghamm, M. D., Brodt, M. D., Lee, K. L., Stephens, A. L., Ye, J., Silva, M. J., Jun. 2010. Age-Related Changes in Bone Structure and Strength in Female and Male BALB/c Mice. Calcified Tissue International 86 (6), 470–483.

You, L., Cowin, S. C., Schaffler, M. B., Weinbaum, S., Nov. 2001. A model for strain amplification in the actin cytoskeleton of osteocytes due to fluid drag on pericellular matrix. Journal of Biomechanics 34 (11), 1375–1386.

PeerJ PrePrints | https://dx.doi.org/10.7287/peerj.preprints.1140v3 | CC-BY 4.0 Open Access | rec: 4 Aug 2015, publ: 4 Aug 2015

List of Figures

PeerJ PrePrints | https://dx.doi.org/10.7287/peerj.preprints.1140v3 | CC-BY 4.0 Open Access | rec: 4 Aug 2015, publ: 4 Aug 2015

PeerJ PrePrints | https://dx.doi.org/10.7287/peerj.preprints.1140v3 | CC-BY 4.0 Open Access | rec: 4 Aug 2015, publ: 4 Aug 2015

PeerJ PrePrints | https://dx.doi.org/10.7287/peerj.preprints.1140v3 | CC-BY 4.0 Open Access | rec: 4 Aug 2015, publ: 4 Aug 2015

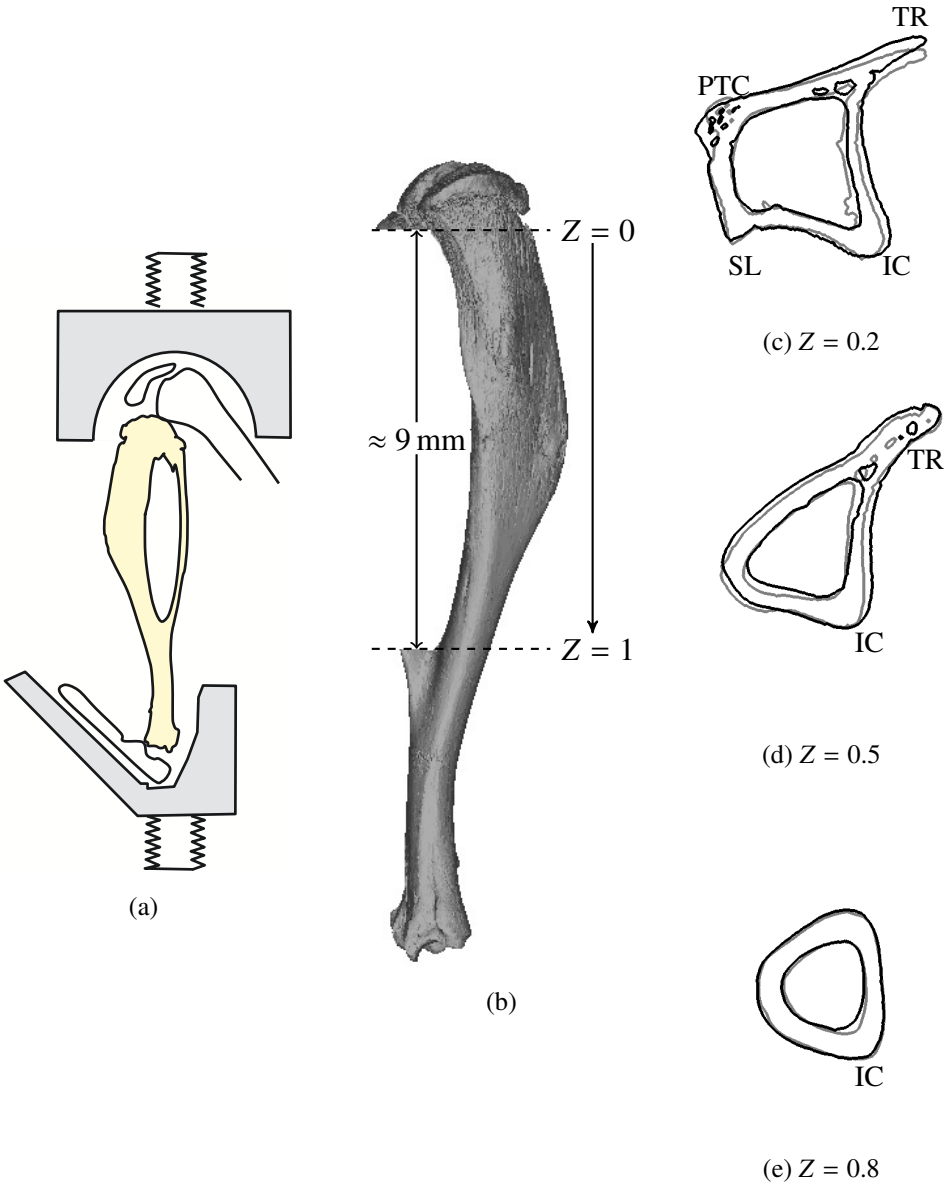

Figure 1: (**a**) The loading model used for this study: axial compression of the murine tibia. (Adapted from De Souza et al. 2005) (**b**) Non-dimensional coordinate, Z, corresponds to the axial space between the proximal ($Z = 0$) and distal ($Z = 1$) tibia-fibula junctions. (**c**–**e**) Cross-section contours of left (non-loaded, grey line) and right (loaded, black line) tibiae for a particular specimen. Anatomical landmarks: interosseous crest (IC), proximal tibial crest (PTC), soleal line (SL), tibial ridge (TR).

PeerJ PrePrints | https://dx.doi.org/10.7287/peerj.preprints.1140v3 | CC-BY 4.0 Open Access | rec: 4 Aug 2015, publ: 4 Aug 2015

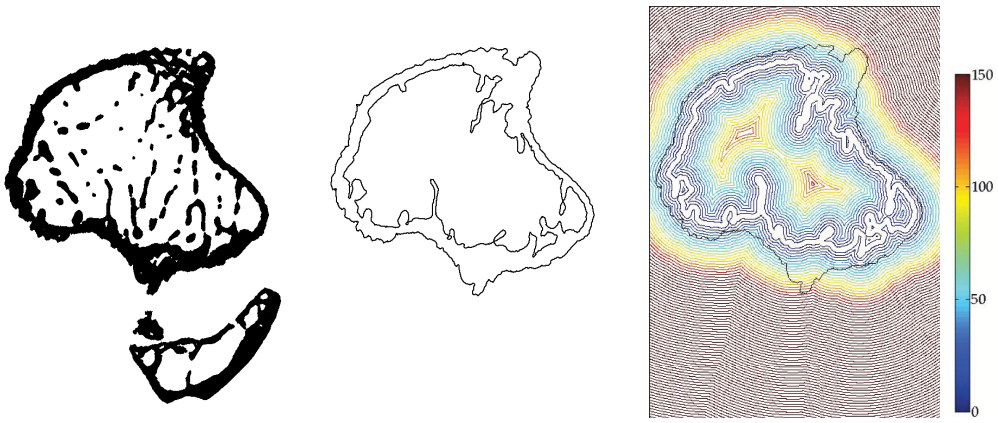

(a) Initial cross-section. (b) Peri- and endosteal boundaries. (c) Map of distances from the endosteum (units in μm).

Figure 2: Steps of script for the calculation of cortical thickness and endosteal distance from centroid.

PeerJ PrePrints | https://dx.doi.org/10.7287/peerj.preprints.1140v3 | CC-BY 4.0 Open Access | rec: 4 Aug 2015, publ: 4 Aug 2015

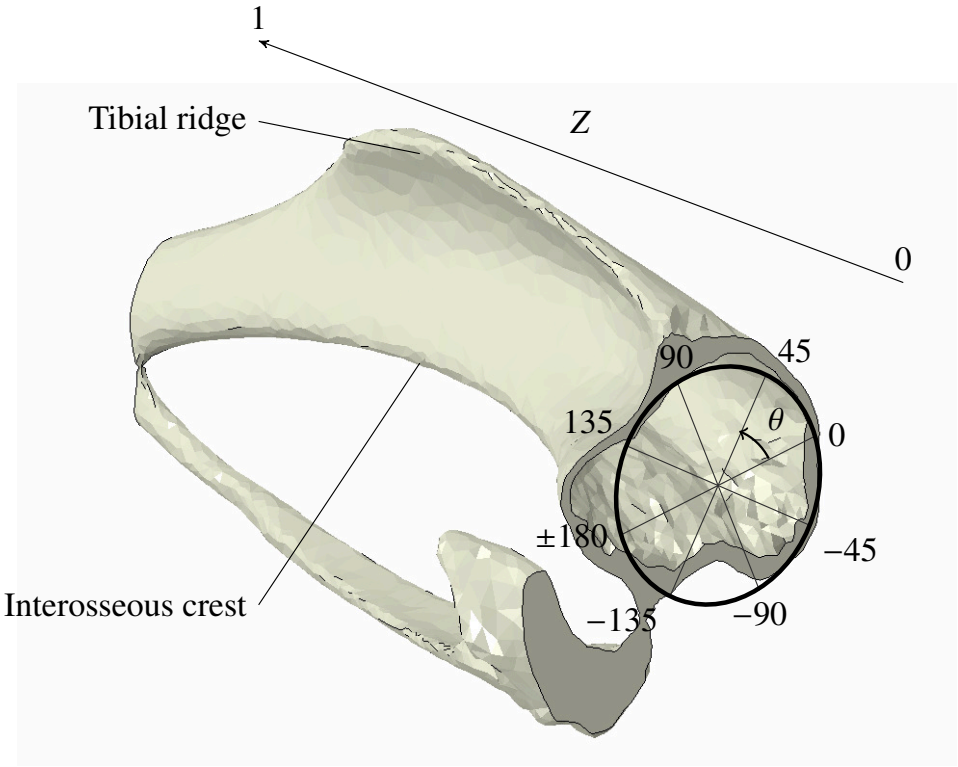

Figure 3: Angular (θ) and longitudinal (Z) coordinates used in the cylindrical coordinates system.

PeerJ PrePrints | https://dx.doi.org/10.7287/peerj.preprints.1140v3 | CC-BY 4.0 Open Access | rec: 4 Aug 2015, publ: 4 Aug 2015

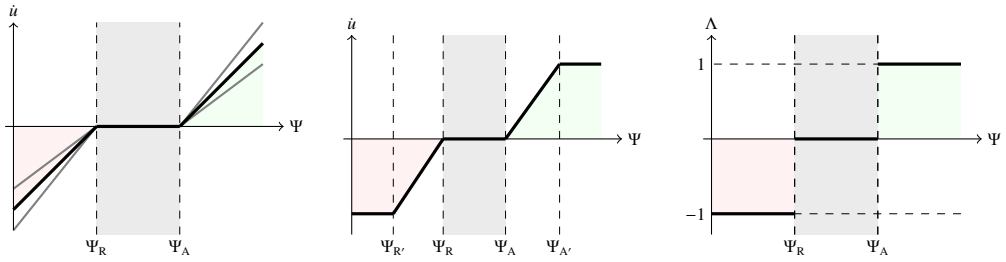

(a) (b) (c)

Figure 4: Different Ψ–$\dot{u}$ (mechanical stimulus *vs.* adaptation) relationship curves considered in this study: (**a**) generic trilinear curve, (**b**) trilinear curved capped with maximum remodelling rates of apposition and resorption, (**c**) On-off relationship. The apposition and resorption limits of the homeosteatic interval, Ψ_A and Ψ_R, dictate the tissue response to mechanical stimulus Ψ. The step curve in (**c**) obtained the most accurate predictions of cortical adaptation.

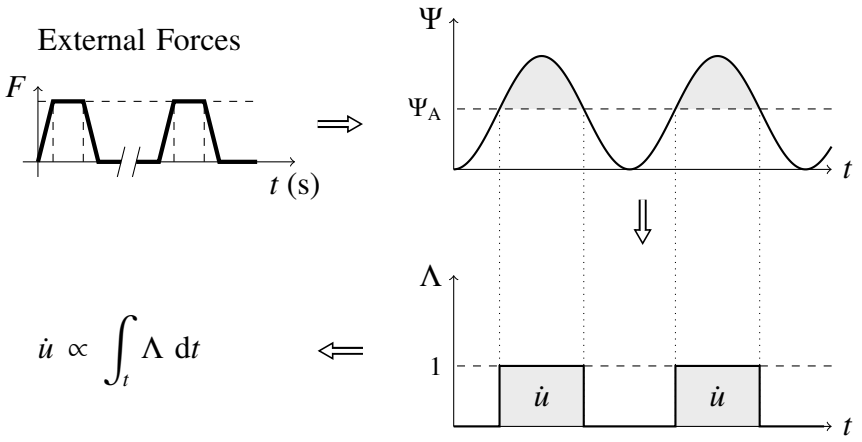

Figure 5: Cortical bone adaptation model: An externally applied force elicits a mechanical signal/stimulus, Ψ, in the bone. If this stimulus is above a certain apposition threshold, Ψ_A, then then an adaptive response is generated ($\Lambda = 1$). This response is integrated over time to give the adaptation rate ($\dot{u}$).

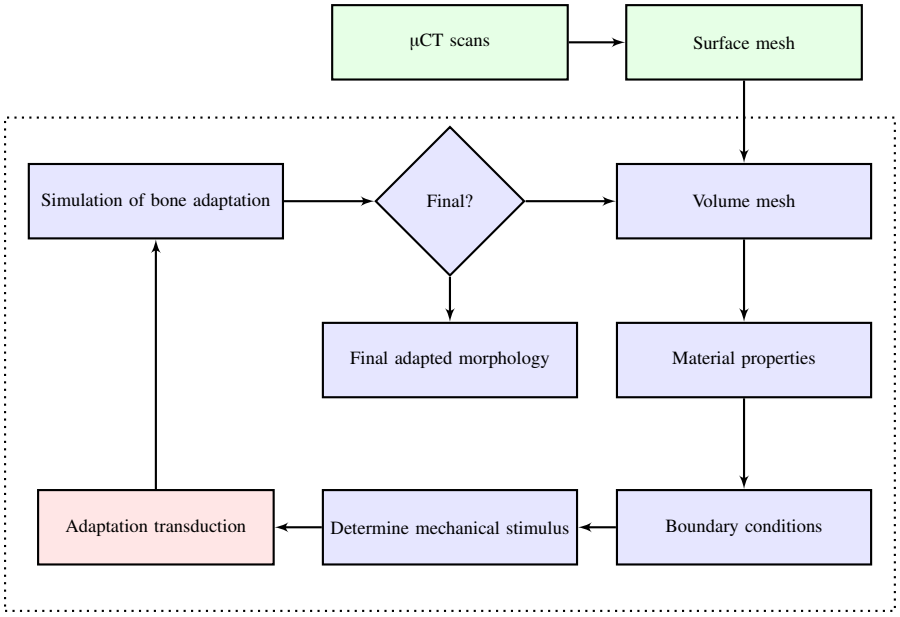

Figure 6: Adaptation algorithm flowchart. Shade indicative of software used: Mimics (green), ABAQUS (blue), MATLAB (red). Steps inside dashed line are automated.

PeerJ PrePrints | https://dx.doi.org/10.7287/peerj.preprints.1140v3 | CC-BY 4.0 Open Access | rec: 4 Aug 2015, publ: 4 Aug 2015

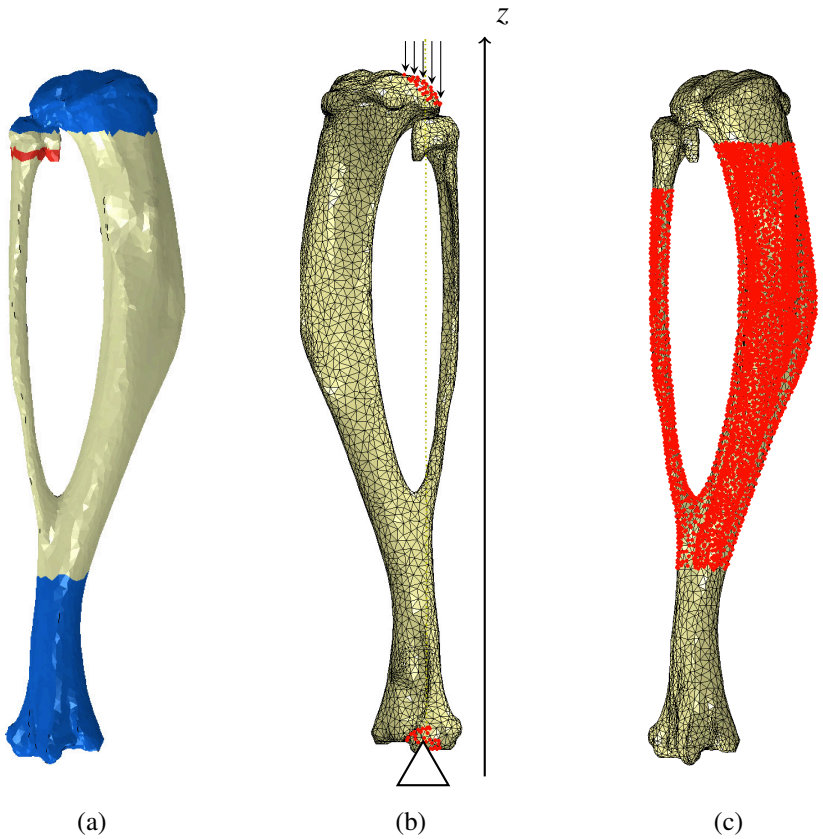

Figure 7: Finite element model used to determine the mechanical environment. (**a**) Medial view of the material sections considered: poroelastic cortical bone (off-white), elastic cortical bone (blue) and fibular growth plate (red), (**b**) Lateral view of the boundary conditions applied and vertical alignment of the model assembly with the z direction, (**c**) Medial view of the region where cortical bone adaptation was considered, demarcated by the cloud of nodes highlighted in red.

PeerJ PrePrints | https://dx.doi.org/10.7287/peerj.preprints.1140v3 | CC-BY 4.0 Open Access | rec: 4 Aug 2015, publ: 4 Aug 2015

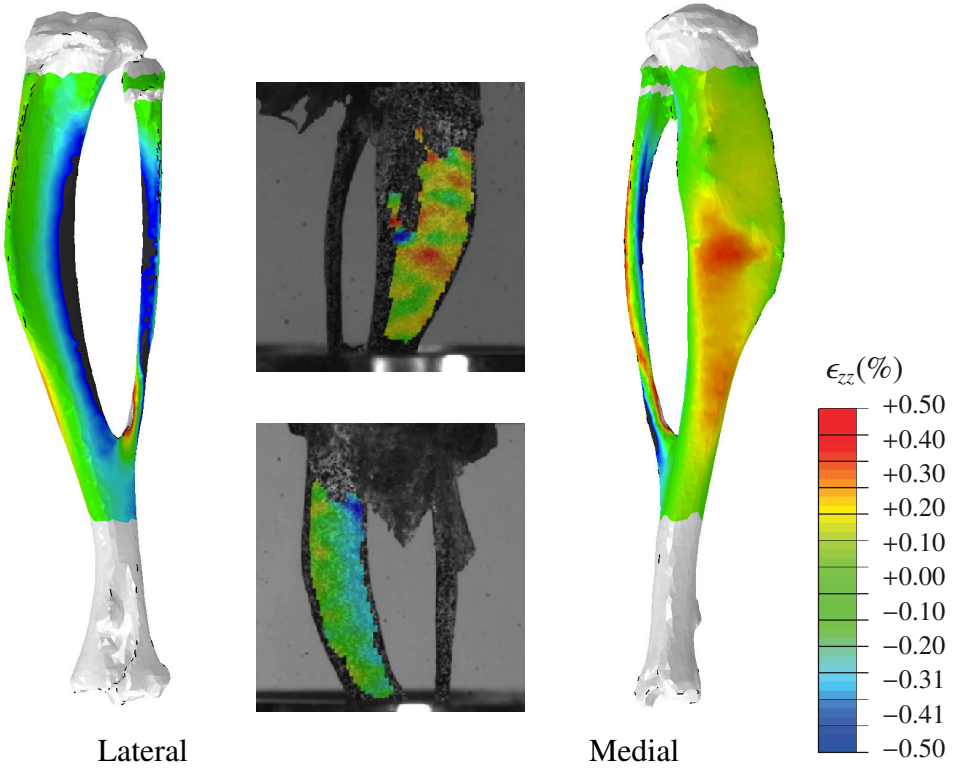

Figure 8: Contour plots of the longitudinal strains ϵ_{zz} calculated in the finite-element models and digital image correlation measurements in 8 week old mice of the same strain and gender by Sztefek et al. (2010). Finite-element analysis used the geometry of a non-adapted under an axial peak load of 12 N. DIC images reprinted from Sztefek et al. 2010 with permission from Elsevier.

PeerJ PrePrints | https://dx.doi.org/10.7287/peerj.preprints.1140v3 | CC-BY 4.0 Open Access | rec: 4 Aug 2015, publ: 4 Aug 2015

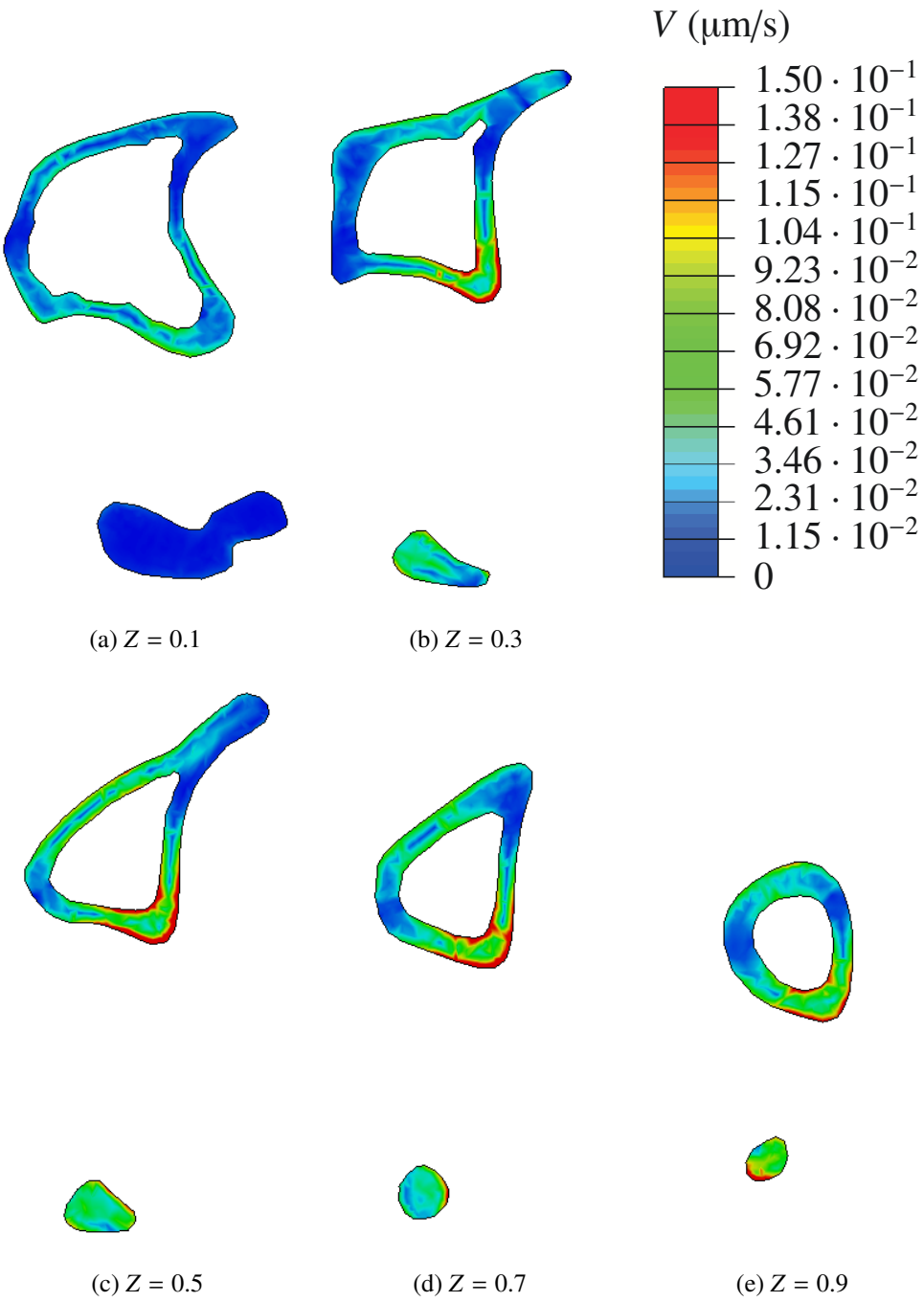

(a) $Z = 0.1$ (b) $Z = 0.3$

(c) $Z = 0.5$ (d) $Z = 0.7$ (e) $Z = 0.9$

Figure 9: Contour plots of fluid velocity, V, obtained at $t = 0.025$s (peak load) for different Z positions in the initial geometry. Higher fluid velocity magnitudes obtained in the medial surface and around the interosseous crest.

PeerJ PrePrints | https://dx.doi.org/10.7287/peerj.preprints.1140v3 | CC-BY 4.0 Open Access | rec: 4 Aug 2015, publ: 4 Aug 2015

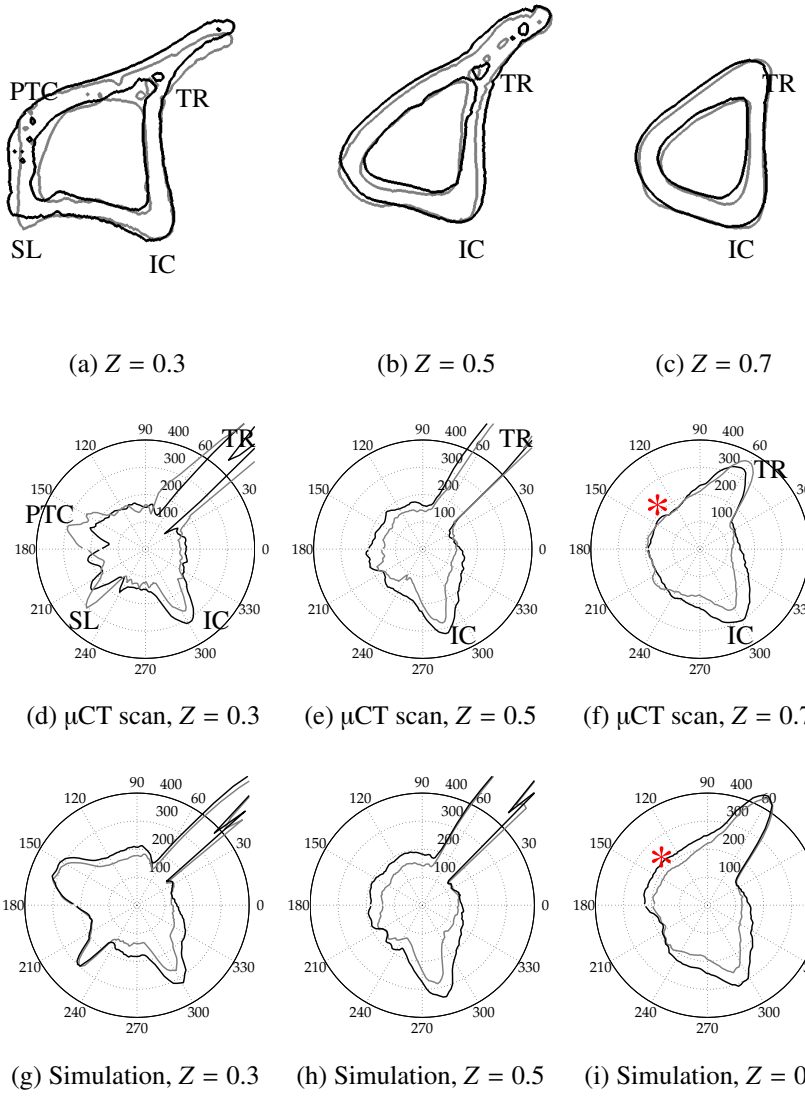

(a) $Z = 0.3$ (b) $Z = 0.5$ (c) $Z = 0.7$

(d) µCT scan, $Z = 0.3$ (e) µCT scan, $Z = 0.5$ (f) µCT scan, $Z = 0.7$

(g) Simulation, $Z = 0.3$ (h) Simulation, $Z = 0.5$ (i) Simulation, $Z = 0.7$

Figure 10: (**a**,**b**,**c**) Cross-section contours of left (non-loaded, grey line) and right (loaded, black line) tibiae, and respective polar representation cortical thickness Th for (**d**,**e**,**f**) the *in vivo* data measurements and (**g**, **h**, **i**) predictions using $\Psi_A = 50$ MPa. The red asterisk (**c** and **i**) is placed at $Z = 0.7$ and $\theta = 135°$ and highlights a region where *in silico* adaptation was overestimated. (Th units in µm)

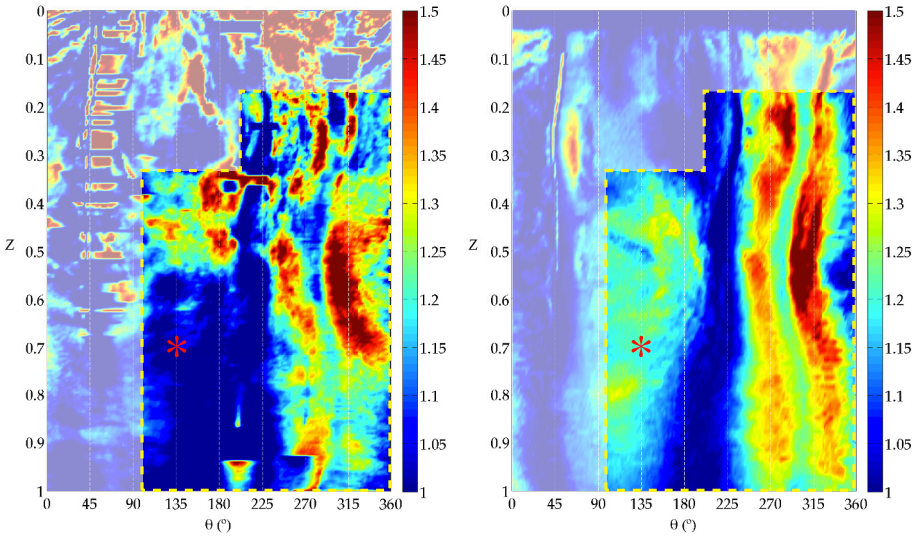

(a) μCT scan (b) Simulation

Figure 11: Color map of changes in cortical thickness $\Delta Th/Th$ measured for *in vivo* data (**a**) against the respective predictions using $\Psi_A = 50$ MPa (**b**). The red asterisk is placed at $Z = 0.7$ and $\theta = 135°$. Artifacts in the experimental data calculations predominate in the region masked over, outside the yellow dashed line.

PeerJ PrePrints | https://dx.doi.org/10.7287/peerj.preprints.1140v3 | CC-BY 4.0 Open Access | rec: 4 Aug 2015, publ: 4 Aug 2015

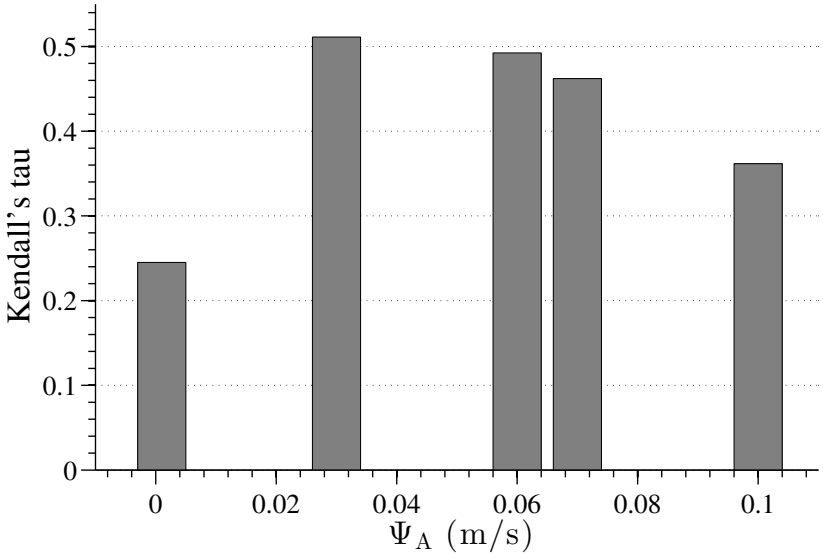

Figure 12: Kendall's tau rank correlation coefficient calculated between *in vivo* and *in silico* $\Delta Th/Th$ measurements obtained for the values of Ψ_A considered in this study. Simulations with an apposition threshold value of $\Psi_A = 3 \times 10^{-2}\,\mathrm{m\,s^{-1}}$ obtained the strongest positive correlation ($p < 0.001$).

PeerJ PrePrints | https://dx.doi.org/10.7287/peerj.preprints.1140v3 | CC-BY 4.0 Open Access | rec: 4 Aug 2015, publ: 4 Aug 2015